

Ultraviolet photochemistry of 2-bromothiophene explored using universal ionization detection and multi-mass velocity-map imaging with a PlmMS2 sensor

R. A. Ingle, C. S. Hansen, E. Elsdon, M. Bain, S. J. King, J. W. L. Lee, M. Brouard, C. Vallance, R. Turchetta, and M. N. R. Ashfold

Citation: *The Journal of Chemical Physics* **147**, 013914 (2017); doi: 10.1063/1.4979559

View online: <http://dx.doi.org/10.1063/1.4979559>

View Table of Contents: <http://aip.scitation.org/toc/jcp/147/1>

Published by the [American Institute of Physics](#)

Articles you may be interested in

[Finite slice analysis \(FINA\)—A general reconstruction method for velocity mapped and time-sliced ion imaging](#)

The Journal of Chemical Physics **147**, 013913013913 (2017); 10.1063/1.4979305

[Time-resolved multi-mass ion imaging: Femtosecond UV-VUV pump-probe spectroscopy with the PlmMS camera](#)

The Journal of Chemical Physics **147**, 013911013911 (2017); 10.1063/1.4978923

[Imaging of rotational wave-function in photodissociation of rovibrationally excited HCl molecules](#)

The Journal of Chemical Physics **147**, 013901013901 (2017); 10.1063/1.4973680

[Advantage of spatial map ion imaging in the study of large molecule photodissociation](#)

The Journal of Chemical Physics **147**, 013904013904 (2017); 10.1063/1.4975671

[A simple resonance enhanced laser ionization scheme for CO via the \$A1\Pi\$ state](#)

The Journal of Chemical Physics **147**, 013909013909 (2017); 10.1063/1.4977986

[Nonadiabatic laser-induced alignment of molecules: Reconstructing \$\langle \cos^2 \theta \rangle\$ directly from \$\langle \cos^2 \theta \rangle\$ by Fourier analysis](#)

The Journal of Chemical Physics **147**, 013905013905 (2017); 10.1063/1.4975817

**PHYSICS
TODAY**

**COMPLETELY
REDESIGNED!**

Physics Today Buyer's Guide
Search with a purpose.

Ultraviolet photochemistry of 2-bromothiophene explored using universal ionization detection and multi-mass velocity-map imaging with a PlmMS2 sensor

R. A. Ingle,^{1,a)} C. S. Hansen,^{1,b)} E. Elsdon,¹ M. Bain,¹ S. J. King,^{2,c)} J. W. L. Lee,² M. Brouard,² C. Vallance,² R. Turchetta,^{3,d)} and M. N. R. Ashfold^{1,e)}

¹*School of Chemistry, University of Bristol, Cantock's Close, Bristol BS8 1TS, United Kingdom*

²*The Chemistry Research Laboratory, The Department of Chemistry, University of Oxford, 12 Mansfield Road, Oxford OX1 3TA, United Kingdom*

³*Rutherford Appleton Laboratory, Chilton, Didcot OX11 0QX, United Kingdom*

(Received 28 February 2017; accepted 20 March 2017; published online 6 April 2017)

The ultraviolet photochemistry of 2-bromothiophene (C_4H_3SBr) has been studied across the wavelength range 265–245 nm using a velocity-map imaging (VMI) apparatus recently modified for multi-mass imaging and vacuum ultraviolet (VUV, 118.2 nm) universal ionization. At all wavelengths, molecular products arising from the loss of atomic bromine were found to exhibit recoil velocities and anisotropies consistent with those reported elsewhere for the Br fragment [J. Chem. Phys. **142**, 224303 (2015)]. Comparison between the momentum distributions of the Br and C_4H_3S fragments suggests that bromine is formed primarily in its ground ($^2P_{3/2}$) spin-orbit state. These distributions match well at high momentum, but relatively fewer slow moving molecular fragments were detected. This is explained by the observation of a second substantial ionic product, $C_3H_3^+$. Analysis of ion images recorded simultaneously for several ion masses and the results of high-level *ab initio* calculations suggest that this fragment ion arises from dissociative ionization (by the VUV probe laser) of the most internally excited C_4H_3S fragments. This study provides an excellent benchmark for the recently modified VMI instrumentation and offers a powerful demonstration of the emerging field of multi-mass VMI using event-triggered, high frame-rate sensors, and universal ionization. © 2017 Author(s). All article content, except where otherwise noted, is licensed under a Creative Commons Attribution (CC BY) license (<http://creativecommons.org/licenses/by/4.0/>). [<http://dx.doi.org/10.1063/1.4979559>]

I. INTRODUCTION

The history of the velocity-map imaging (VMI) technique spans two decades,^{1–3} yet new chapters are still being written as technological developments continue to extend the power and versatility of the technique. One area in which this is perhaps most evident is the advent of event-triggered, high frame rate sensors. These devices are able to acquire bursts of images with time resolutions on the order of tens of nanoseconds and address some longstanding challenges of velocity-map imaging. A prominent theme in the development of the VMI technique is how to record the two-dimensional (2-D) projection from the complete three-dimensional (3-D) velocity distribution of a mass-selected (by time-of-flight (TOF)) ensemble of ions. Frequently, these ions are the products of photodissociation^{4–7} or scattering reactions,^{8–12} and evolve as expanding concentric spheres (Newton spheres) with radii

proportional to their recoil velocities. Typically, these spheres are crushed onto a position-sensitive detector and one attempts to reconstruct the central slice mathematically.^{13–16} Such approaches often add artefacts to the central line of the recovered image and are only suitable when the 3-D distribution is cylindrically symmetric. Consequently, a number of approaches have been developed that use optical^{17–20} or electrostatic^{17,18,21–24} tools to measure slices of the 3-D velocity distribution directly. For cylindrically symmetric distributions, an approximation of the central slice of the 3-D distribution can be measured, without the need for mathematical reconstruction. In other cases,²⁵ the entire 3-D distribution can be recorded by “stepping” through the TOF arrival times. In all of these approaches, however, the frame rate of the sensor (typically a charge-coupled device, CCD) limits the acquisition rate to once per TOF cycle, i.e., simply recording the image for one TOF arrival time per experimental cycle. This is a time-consuming process that is sensitive to experimental drift during acquisition.

Some of the above limitations can be overcome by detecting the spatial and temporal coordinates of the ion impacts simultaneously, allowing the entire 3-D velocity distribution to be measured in one experiment. The earliest experiments of this type were based on delay-line anodes.^{26,27} Simply, these devices comprise wires wound about a 2-D surface. By measuring the time it takes for electrons formed as a result of an

^{a)}R. A. Ingle and C. S. Hansen contributed equally to this work.

^{b)}Author to whom correspondence should be addressed. Electronic mail: christopher.hansen@bristol.ac.uk

^{c)}Present address: School of Chemistry, Purdie Building, North Haugh, St. Andrews, United Kingdom.

^{d)}Present address: WegaPixel, c/Baldiri Reixac, 4-12 i 15, 08028 Barcelona, Spain.

^{e)}Author to whom correspondence should be addressed. Electronic mail: mike.ashfold@bristol.ac.uk

ion impact to reach both ends of the wire, the arrival time and position of the impact can be determined precisely (within 100 ps and 100 μm).²⁸ However, delay-line anodes suffer from considerable dead-time following an event and can typically only image a few ions per TOF cycle. Even more complex designs are limited to detecting up to 100 ions,²⁹ which is still too few for typical 3-D VMI experiments.

More recent solutions are pixel based and can operate at higher signal levels. This is because each pixel records the time an ion is detected and its spatial information comes from the identity of the reporting pixel, rather than the location of the impact within the pixel. Such sensors effectively work as an array of delay lines. Suitable devices have been developed by incorporating multiple memory registers into each pixel of a CCD camera.^{30,31} However, such devices exhibit decreased light sensitivity and generate enormous amounts of data, mostly zeroes, as full frames need to be transferred ultimately lowering the maximum frame rate. Another recent pixel based approach involves operating a fast frame camera in tandem with a photomultiplier tube (PMT) whereby the precise timing information from the PMT is used to refine the spatial and temporal coordinates recorded by the camera.^{32,33} This approach can achieve resolutions of ~ 100 ps and ~ 100 μm . However, the need to pair events from both detectors, as well as the fact that the PMT can detect events that the camera cannot, necessitate a lower event count that makes it better-suited to coincidence-based measurements.

One recent development that addresses all the aforementioned challenges is the emergence of event-triggered, high frame rate sensors. These sensors are CMOS (complementary metal-oxide semiconductor)-based and consist of an array of independent pixels each containing multiple memory registers. These pixels are triggered at the beginning of a TOF cycle, at which point they begin counting. Once a pixel detects a signal above a user-defined threshold, the position and the time of the event are recorded. Such sensors are built on a number of architectures and include the Pixel Imaging Mass Spectrometry (PIImS)³⁴ and TimePix families.³⁵ The PIImS2 sensor is used in the present study and is the only one discussed further. Its spatial resolution is 324×324 pixels, each containing four memory registers capable of reporting ion events with a time resolution of 12.5 ns.

PIImS2 allows the entire 3-D velocity distribution to be recorded, and sliced through, for every ion in the TOF mass spectrum, i.e., multi-mass imaging. This can drastically reduce the time an experiment takes if multiple TOF arrival times need to be studied. It also eliminates the effect of experimental drift, as every ion image for every mass channel is recorded at the same time and under the same set of experimental conditions. Rich photochemistry can thus be studied with no prior knowledge of the resulting fragments. In fact, as we show in the present work, a minor product channel (m/z 44, CS^+) unnoticed during data acquisition can be identified and analyzed post-completion of the data collection. PIImS sensors are an emerging technology but have already been used to acquire multi-mass velocity-map images following photolysis of carbon disulfide (CS_2) and dimethyl disulfide ($\text{H}_3\text{CS}_2\text{CH}_3$),³⁶ carbonyl sulfide (OCS) and methyl iodide

(CH_3I),^{37,38} ethyl iodide,³⁸ molecular bromine (Br_2), and N,N -dimethylformamide ($\text{CH}_3)_2\text{NCHO}$ ³⁹—yielding results in agreement with those acquired using conventional CCD cameras.³⁷

Conventional VMI experiments image one TOF arrival time and can benefit from a detection scheme, typically resonance enhanced multiphoton ionization (REMPI),⁴⁰ optimized for a particular atomic or molecular species and often in a specific quantum state. However, multi-mass VMI techniques are particularly powerful when coupled to universal ionization methods that ionize all products of a reaction and take advantage of the entire TOF cycle. Notwithstanding the loss of state-specific information, this can often be advantageous when product state information is retained in the image or when signal levels are too low to forgo sampling the full manifold of quantum states. One such approach is to use a laser source with a photon energy that exceeds the ionization potential (IP) of most, or preferably, all species of interest. Recognised examples that have already found use in VMI studies include the vacuum ultraviolet (VUV) wavelengths from a fluorine excimer laser (157 nm),^{41,42} the 9th (118.2 nm, 10.5 eV) or 12th (88.7 nm, 14 eV) harmonics of a Nd:YAG laser,^{38,43} or if greater tunability is required, wavelengths generated by two-color four-wave mixing methods (e.g., 125 nm).⁴⁴ Each of these ionization sources is to some extent “universal” and in favourable cases results in low amounts of dissociative ionization ‘soft ionization’. However, as shown in the present manuscript, this will not always be the case, and dissociative ionization can still be a major channel. When using a laser, however, the photon energy is sufficiently well defined to permit analysis of the products of the dissociative ionization process, thereby revealing additional details about the photochemistry of the target molecule. This is in contrast to more truly “universal” detection methods like electron impact (EI), for which it is difficult to precisely define the incident electron energy or to minimise large amount of unwanted fragmentation.

This study builds directly on the aforementioned developments. An event-triggered PIImS2 sensor and VUV laser source are coupled to a pre-existing VMI experiment to investigate the ultraviolet photochemistry of 2-bromothiophene ($\text{C}_4\text{H}_3\text{SBr}$, the sulfur analogue of 2-bromofuran) across the wavelength range $265 \geq \lambda \geq 245$ nm ($37\,736\text{--}40\,816$ cm^{-1}). This extends a recent ion imaging study in which the photochemistry of 2-bromothiophene was explored over the same wavelength range in a conventional VMI experiment by monitoring just the atomic bromine fragments.⁴⁵ This earlier work revealed two wavelength-dependent photodissociation channels: one yielding fast bromine fragments with an anisotropic velocity distribution (which was dominant at $\lambda > 260$ nm) and a slow, isotropic channel which grew in relative importance and eventually dominated at shorter UV wavelengths. The manifold of excited electronic states was explored with high-level *ab initio* calculations, and the authors concluded that the fast channel that dominates at longer excitation wavelengths arises from the direct population of a $n\sigma^*$ -excited state that is dissociative with respect to C-Br bond extension. At shorter wavelengths, however, the dominant absorption is to a diabatically bound $\pi\pi^*$ excited state. The calculations

suggest that internal conversion (IC) from this state, via elongation of the C-S bond, offers a route to internally activated, ring-opened, ground state species which then undergo unimolecular decay, liberating a slow Br atom. Such photochemical ring-opening mechanisms are of general interest and should be rather common. They have been postulated for a number of sulfur-containing heterocyclic species, in both the gas and condensed phases,^{45–49} but conclusive observations remain rare and are generally limited to solution phase studies.^{50,51}

The present study was conceived in the expectation that the dynamics of the cofragment formed upon C-Br bond fission, and of any lighter mass fragments, would provide additional insights into this striking wavelength-dependent shift in photophysical behaviour and perhaps provide additional evidence for the ring-opening pathway. This system also provides a benchmark for the recently modified VMI apparatus (which is detailed here for the first time) and is an excellent demonstration of the future potential of combining multi-mass VMI using a PImMS sensor and VUV ionization.

This manuscript reports ion images for the C_4H_3S fragments formed by Br-loss from 2-bromothiophene, which are pleasingly similar to those recorded previously for the Br partner.^{45,52} The high end of the momentum distribution of the Br-loss fragment agrees well with that measured for the Br atom in its $^2P_{3/2}$ spin-orbit state, suggesting that this is the major product channel. At low momentum, however, the Br-loss fragment appears under-detected relative to expectations based on the measured Br atom distributions. This we attribute to dissociative ionization of the C_4H_3S species, forming the lighter $C_3H_3^+$ ion. This conclusion is supported by the simultaneously recorded images of the $C_3H_3^+$ ion, which link both fragment ions to a common origin, and by the wavelength-dependent branching fractions determined from the TOF mass spectra that reveal an increasing probability for forming the lighter species at shorter wavelengths. The ion images, supported by energetics calculations, predict this dissociative ionization channel to be accessible to $\sim 24\%$ of the C_4H_3S products formed at the longest wavelength used in this study (265 nm).

II. METHODS

A. Experimental methods

The velocity-map imaging apparatus has been described in detail elsewhere,⁵³ and only an overview is provided here. Particular attention is given to the description of any recent modifications. The molecular beam was generated by a 0.5 mm orifice pulsed valve (General Valve Series 9 driven by an Iota One valve driver) mounted on a source chamber and aligned to a 1 mm orifice skimmer. The molecular beam then passed through the skimmer into a differentially pumped photolysis chamber where it travelled along the principal axis of a recently redesigned ion optics assembly.⁴⁵ This assembly fits inside a grounded, liquid nitrogen-cooled cryoshield and comprises four custom electrodes optimised for velocity-map imaging including a “top-hat”-

shaped repeller electrode and an extractor electrode with a carefully designed spherical surface facing the interaction volume. This new setup provides a (simulated) five-fold increase in velocity resolution over the previously incorporated electrode arrangement.

The early time component of the pulsed molecular beam was intersected between the repeller and extractor electrodes by the ultraviolet photolysis (pump) laser: a Sirah Lasertechnik Cobra-Stretch with a 2400 grooves mm^{-1} grating pumped by the third harmonic (355 nm) of a 10 Hz, nanosecond Nd:YAG laser (Spectra-Physics GCR-250). Coumarin 503 (Coumarin 307) dye was used to generate all photolysis wavelengths in this study. The $\lambda = 1064$ nm output of the Nd:YAG laser was attenuated before third harmonic generation using a $\lambda/2$ waveplate to yield ~ 80 mJ of $\lambda = 355$ nm light resulting in 0.5–1.0 mJ of UV frequency-doubled dye laser output, which was then directed (unfocused, diameter ≈ 2 mm) into the vacuum chamber using two 90° quartz prisms. Following a 25 ns delay, the molecular beam was then intersected by a counter-propagating $\lambda = 118.2$ nm (henceforth 118 nm) VUV “universal ionization” (probe) laser reported here for the first time and detailed in Section II A 1.

The resulting cations were then accelerated through the ion optics assembly and mass separated along a 460 mm field-free TOF region before impacting upon a new MCP detector and ultimately being recorded by a fast CMOS image sensor (PImMS2); both are described in Sec. II A 1.

2-bromothiophene (98%) was purchased from Sigma-Aldrich. Approximately 2 ml of sample was pipetted into the cold finger of a 1 L Pyrex bulb. This aliquot was then degassed by four freeze-pump-thaw cycles using liquid nitrogen, at which point no bubbles evolved from the solution upon thawing. The cold finger was then submerged into a constantly maintained cooling bath of ice and water ($0^\circ C$) to lower its vapor pressure, which was then seeded in 700 mbar of helium (N5.2 grade, BOC). The sample bulb was then covered in opaque low-density polyethylene to prevent any unwanted photochemistry. To ensure an established vapor pressure and mixing of the gases, the sample was then allowed to stand for 30 min before being introduced into the experiment as described above.

Each experiment comprised 20 000 laser shots except when the photolysis wavelength was 255 nm, where the data appeared clearly converged after 10 000 laser shots. Experiments monitoring atomic Br signals used the dye laser for both the photolysis of 2-bromothiophene and the $(2 + 1)$ REMPI ionization of the Br fragments. Ground ($^2P_{3/2}$) and spin-orbit excited ($^2P_{1/2}$) Br atoms were detected via the $4p^45p^1\ ^4D_{3/2}$ intermediate state (using a photon energy of $38\,371.54\text{ cm}^{-1}$) and the $4p^45p^1\ ^2P_{1/2}$ level (following excitation at $\tilde{\nu} = 38\,091.40\text{ cm}^{-1}$), respectively. To ensure equal sensitivity to fragments with all velocities, the frequency-doubled dye laser output was repeatedly scanned ± 0.02 nm across the centre of the REMPI transition. All data in the present study were recorded with a consistent set of electrode voltages, which were calibrated for ion velocity by monitoring the Br ($^2P_{3/2}$) signal from the UV photolysis of molecular bromine (Br_2) before and after acquiring the data reported herein.

As this experiment saw a new detector, sensor, and ionization source implemented for the first time, preliminary data (TOF mass spectra and representative ion images) were recorded using a different VMI apparatus and CCD camera. This experiment has also been described elsewhere.⁵⁴ An overview and some of the preliminary data are presented in section A of the [supplementary material](#).

1. Detector and PImMS2 sensor

The detector was a customized Photek VID340 open face vacuum detector. It comprised three 40 mm (active diameter) microchannel plates (MCPs), providing a gain of 10^8 – 10^9 , and a $\text{Y}_2\text{SiO}_5\text{:Ce}$ (P47) phosphor-coated scintillator mounted on a 6 in. stainless steel flange. Although the use of a high frame rate sensor should remove the need for detector time-gating, it is still advantageous to exclude signals such as those arising from scattered laser light, intact parent molecules, and carrier gases to prolong the life of the detector. The electronics of the detector have been customized accordingly. The front (facing the vacuum) two MCPs are impedance matched, and a bias is applied across both, while the voltage across the rear channel plate can be configured independently. Fixed voltages were provided by a Photek DPS3-VID three output, high voltage power supply. When full sensitivity was required, a +500 V square pulse is applied to the rear MCP by a Photek GM-MCP-2 gate module customized to have a heightened (+2300 V) trip level. For the experiments reported here, the detector was maintained at full sensitivity for TOF arrival times spanning m/z 5–90—excluding the signals from scattered laser light, helium carrier gas (m/z 4), and intact parent molecules. Typical voltages at full sensitivity were +1400 V across the front two channel plates, +700 V across the rear channel plate, and +4000 V between the back face of the rear channel plate and the phosphor screen.

The PImMS2 camera housing was fastened to an x , y , z translation mount positioned outside the vacuum chamber approximately 200 mm from the phosphor screen. A Nikon Micro NIKKOR 55 mm S-mount macro lens ($f/2.8$) was used to ensure that the image of the scintillator filled the PImMS2 sensor and was focused. A thermoelectric module maintained the sensor at a temperature of 17.5 °C resulting in a dark signal count of 80 ions spread over the entirety of the detector and all 4096 time bins. The camera was operated at a rate of eight cycles per time code corresponding to a time resolution of 25 ns and about 100 μs of acquisition time per frame. Data were recorded using a LabVIEW interface as a three dimensional list of ion events (x , y and t) indexed by frame number.

2. Vacuum ultraviolet laser light source

The generation of 118 nm laser light employs a custom 500 mm long stainless steel cell with 0.75 in. outside diameter. This cell is sealed at one end by a quartz viewport and at the other by a custom LiF lens ($f = 138.6$ mm, Eksma Optics) coupled directly to the ion imaging vacuum chamber. The cell is filled with a ~1:12 phase-matched mixture of xenon (N5.0 grade, BOC) and argon (N6.0 grade, BOC). Mixing of the gases and condensation of impurities

is driven by a cooling bath, fixed to a convection loop on the side of the cell, containing a dry ice and methanol slush bath (−78 °C).

To generate the VUV light, this gas cell is pumped by the third harmonic (355 nm) of a 10 Hz, nanosecond Nd:YAG laser (Continuum Surelite I) attenuated by an extended Q-switch delay to output approximately 10 mJ per laser pulse. This light is focused before entering the gas cell using a fused silica lens with a focal length of 300 mm. The residual 355 nm light and the generated 118 nm light then pass through the LiF lens into the vacuum chamber. The residual 355 nm light is of insufficient intensity to yield products of three-photon ionization, as verified by the complete disappearance of signal following even small changes to the Xe:Ar ratio.

3. Analysis

Data from the PImMS2 sensor are recorded as a list, in time and space, of ion events. From these lists, the TOF mass spectrum (TOF-MS) and all ion images can be extracted from a single measurement. First, the TOF-MS was constructed, at each wavelength, by simply counting the number of events occurring at each 25 ns increment. Typically, the TOF signal associated with a given ion mass spanned approximately ten 25 ns time bins, and velocity-map images were prepared for each mass channel by graphing the x and y intensities occurring within its central 25 ns-wide time bin. It has been shown that this method yields velocity distributions in agreement with those determined by mathematically reconstructing the central slice of a crushed image using a conventional CCD camera.³⁷ The central slices prepared directly in this manner were satisfactory. However, as in traditional imaging experiments, a single ion can illuminate multiple pixels on the sensor. This is more complicated in multi-mass imaging experiments whereby a single ion event can also appear across a range of times. To improve the resolution of the ion images, in time and space, a centroiding algorithm was implemented. This algorithm is described in detail elsewhere.³⁷ Briefly, the code searches through the ion events for those occurring adjacent to one another (i.e., $\Delta x = \pm 1$ pixels and/or $\Delta y = \pm 1$ pixels) and within a range of times, Δt . In the present study a time range of $\Delta t = 100$ ns (4 time bins) was used. Clusters of nearby events are then centroided in space to their centre-of mass and in time to that of their earliest detected event. Ion images prepared for $\text{C}_4\text{H}_3\text{S}^+$ were not centroided as they exhibited too much overlapping signal for the technique to be valid. Finally, the images were symmetrized to account for inhomogeneities in the detector sensitivity and to improve the signal-to-noise ratio.

Radial integration and anisotropy parameter determination for the sliced ion images employed the Slimmer LabVIEW VI.⁵⁵ Total kinetic energy release (TKER) calculations for the $\text{C}_4\text{H}_3\text{S}$ fragment assume a mass of 79.92 Da for the bromine cofragment consistent with the natural abundance of its stable isotopes.

B. Computational methods

Geometry optimisations were carried out at the RI-MP2/def2-TZVP^{56–58} level of theory using the TURBOMOLE

V6.2⁵⁹ software package. Single-point energies were then calculated in Molpro 2010.1⁶⁰ for these optimised geometries using CCSD(T)-(F12*)/aug-cc-PVTZ⁶¹ for the closed-shell species or UCCSD(T)-(F12*)/aug-cc-PVTZ⁶² for open-shell species.

III. RESULTS AND DISCUSSION

A. Time-of-flight mass spectrometry

Multi-mass imaging experiments were conducted on jet-cooled 2-bromothiophene across the wavelength range 265–245 nm. Several fragment ions were detected at all these wavelengths, and a representative TOF-MS is presented in Fig. 1. This mass spectrum was acquired over the m/z range 35–90 with a photolysis wavelength of 255 nm and exhibits behaviours observed throughout the photon energy range investigated in this work. The expected $C_4H_3S^+$ ion, resulting from the homolysis of the C–Br bond in 2-bromothiophene and subsequent photoionization, is present at m/z 83. However, it is not the dominant ion detected at this photolysis wavelength. The base peak appears at m/z 39, consistent with formation of $C_3H_3^+$. It will later be shown that this channel can be attributed to the VUV-radiation induced dissociative ionization of the primary C_4H_3S fragments from 2-bromothiophene. Three minor channels are revealed by the appearance of small yields of ions with m/z 44, 56, and 57 assigned as CS^+ , $HCCS^+$, and H_2CCS^+ , respectively. Note that the m/z 56 and 57 species are partially resolved in Fig. 1. This is only the case for the TOF-MS prepared using the aforementioned centroiding algorithm, which centers clusters of ion events in spatial and temporal coordinates. Mass spectra prepared from the raw ion events list exhibit a single feature spanning m/z 56–57. No fragment ions with $m/z > 83$ were detected.

Although the ions labelled in Fig. 1 were observed at all photon energies, the partitioning amongst them varied with wavelength. This is illustrated in Fig. 2, which plots the TOF-MS branching fraction of each channel as a function of wavelength. The x -axis has been scaled to be linear in photon energy, and the error bars represent a confidence of 95% (2σ). Lines are drawn through the data merely to guide the eye. Such analyses with conventional VMI equipment may be challenging or time-consuming given the need to account for changes or

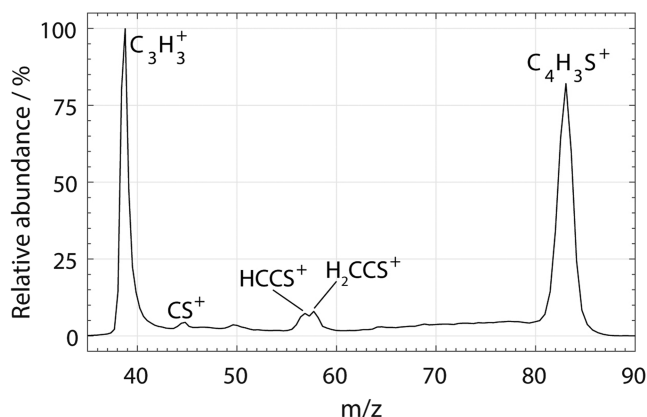


FIG. 1. Time-of-flight mass spectrum recorded between m/z 35–90 following the UV excitation ($\lambda = 255$ nm) and VUV ($\lambda = 118$ nm) ionization of a jet-cooled sample of 2-bromothiophene in helium.

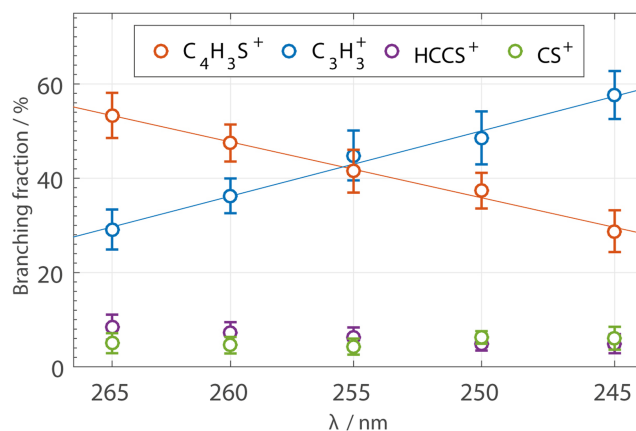


FIG. 2. Wavelength-dependent branching fractions for the UV ($\lambda = 265$ –245 nm) photodissociation products of 2-bromothiophene detected by 118 nm photoionization. The x -axis is linear in photon energy, and the error bars represent a confidence of 95% (2σ).

drifts in experimental conditions. However, a sensor such as PImMS2 forgoes the need to time-gate the detector. These branching fractions will be drawn on later when interpreting the ion images, as they are prepared from the same lists of ion events.

These wavelength-dependent branching fractions reveal a striking linear decrease in the $C_4H_3S^+$ branching fraction (orange) with increasing photon energy. Further, it appears that the decreasing $C_4H_3S^+$ yield matches the (linear) increase of the $C_3H_3^+$ ion yield (blue). This trend will be discussed further in Section III E and is attributed to the dissociative ionization of the most internally excited C_4H_3S fragments. The much less abundant CS^+ and $HCCS^+$ ions also display a similar trend, whereby the $HCCS^+$ ion comprises a larger fraction of the ion fragments detected at long wavelengths, but is relatively less abundant (cf. CS^+) at higher photon energies. This trend, however, is less significant than the statistical uncertainty.

B. Velocity-map imaging

Just as TOF-MS and branching fractions can be determined from the list of ion events recorded by the PImMS2 sensor, so too can ion images for any TOF arrival time of interest. Fig. 3 presents the ion images and respective TKER distributions recorded at each of the experimental photolysis wavelengths for the $C_4H_3S^+$ ion. The laser polarization vector is vertical in the plane of the images as illustrated in Fig. 3(a). Because these signals represent the C_4H_3S fragment recoiling from both stable isotopes of atomic bromine, the TKER calculations assume a mass of 79.90 Da for the Br cofragment. The vertical arrows indicate the maximum TKER ($TKER_{max}$) determined as the point where the intensity on the high energy end of the distribution has decreased to 10% of its maximum value. These images and TKER distributions exhibit minor differences but are generally similar to those reported previously for the atomic bromine cofragments arising from the photolysis of 2-bromothiophene at similar wavelengths.⁴⁵

Fig. 3(a) was recorded at the longest photolysis wavelength used in the present study, $\lambda = 265$ nm. The ion image is dominated by a fast, anisotropic component aligned parallel

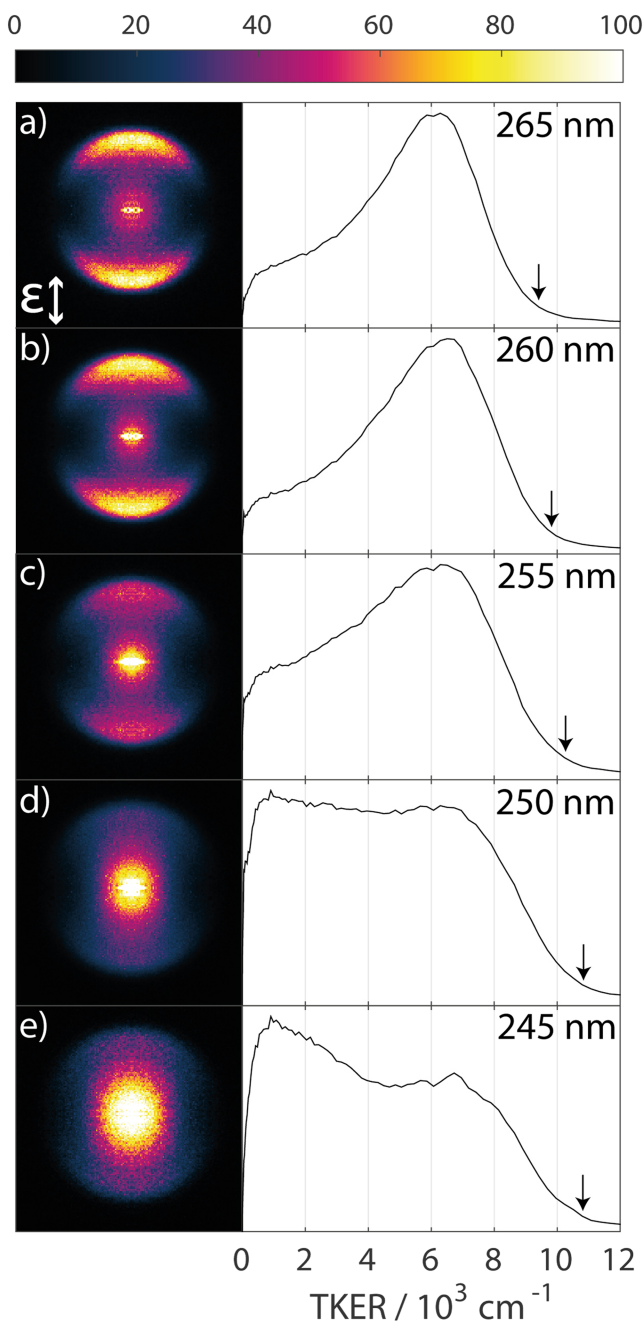


FIG. 3. Velocity-map images of the $\text{C}_4\text{H}_3\text{S}^+$ ions detected by vacuum ultraviolet ionization ($\lambda = 118$ nm) following the ultraviolet irradiation of jet-cooled 2-bromothiophene at $\lambda =$ (a) 265 nm, (b) 260 nm, (c) 255 nm, (d) 250 nm, and (e) 245 nm. The photolysis laser polarization vector (ϵ) is vertical in the plane of the images and illustrated in panel (a). The TKER distributions of the Br + $\text{C}_4\text{H}_3\text{S}$ fragments derived from these images are shown alongside. Arrows in the TKER distributions mark the maximum TKER as the point where the intensity on the high energy end of the distribution has decreased to 10% of its maximum value.

to the photolysis laser polarization axis with a near-limiting anisotropy parameter of $\beta \sim 1.8$. This is in accord with previous studies and reflects the alignment of the transition dipole moment, μ , along the C–Br bond.⁴⁵ The centre of the image also reveals a minor, translationally slow component elongated in the direction of laser propagation. This oval-shaped perturbation persists at all photolysis wavelengths and is attributed to space-charging in the interaction volume by undetected precursor molecules ($\text{C}_4\text{H}_3\text{SBr}$) also ionized by the $\lambda = 118$ nm

radiation. The TKER distribution is dominated by a fast component, centred at TKER ~ 6000 cm^{-1} , with a TKER_{max} that is consistent with the previously reported bond dissociation energy ($\sim 29\,000$ cm^{-1}),⁴⁵ *q.v.* Section III D. Fig. 3(b) shows the $\text{C}_4\text{H}_3\text{S}^+$ ion image recorded at $\lambda = 260$ nm, along with the TKER distribution derived therefrom. These are almost unchanged from those in Fig. 3(a). The image continues to be dominated by a fast, anisotropic component that is, again, centred at TKER ~ 6000 cm^{-1} .

The image acquired at $\lambda = 255$ nm (Fig. 3(c)) reveals a change in the behaviour. Two features are now evident in the TKER distribution: the fast component, again centred at TKER ~ 6000 cm^{-1} , and a slow component that peaks at TKER values close to zero. This trend continues as the photolysis wavelength is reduced. The image in Fig. 3(d) ($\lambda = 250$ nm) appears much more isotropic, and the TKER distribution shows the “fast” and “slow” channels having almost equal intensities. By $\lambda = 245$ nm, the slow component dominates both the ion image and the resulting TKER distribution. Note that the TKER_{max} predicted in the same way as above is almost unchanged from that for $\lambda = 250$ nm (Fig. 3(d)), suggesting that these values are less reliable when the slow channel dominates the TKER distribution. Despite these stark changes in the photodissociation dynamics, the peak of the fast component in the TKER distribution shifts little across Figs. 3(a)–3(e), remaining at TKER ~ 6000 cm^{-1} . This suggests that the average TKER associated with these “fast” products is essentially independent of photolysis wavelength and that increasing the photon energy leads to an increase in the internal energy of the $\text{C}_4\text{H}_3\text{S}$ fragment (rather than the fragment translational energy). This point is critical to many of the key conclusions of this study, and will be referred to throughout the discussion.

The C_3H_3^+ ion (m/z 39) was the other major fragment ion observed following UV photolysis of 2-bromothiophene and subsequent $\lambda = 118$ nm VUV ionization. Images for the C_3H_3^+ ions, extracted from the same ion event lists used to construct Figs. 3(a), 3(c), and 3(e), are presented in Fig. 4. The mechanism for C_3H_3^+ ion formation is less clear than in the case of C–Br bond homolysis, so TKER distributions have not been determined from these images. However, the C_3H_3^+ recoil velocity distributions and anisotropies are reminiscent of those for the $\text{C}_4\text{H}_3\text{S}^+$ ions measured at the same wavelengths (Fig. 3) and provide insight into the likely C_3H_3^+ formation mechanism. The m/z 39 ion image recorded following 265 nm excitation (Fig. 4(a)) shows a fast component recoiling preferentially along the axis parallel to the laser polarization vector.

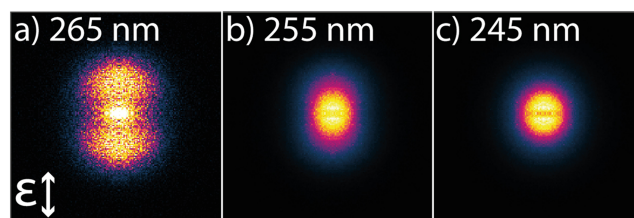


FIG. 4. Velocity-map images of the C_3H_3^+ ions detected by VUV ionization ($\lambda = 118$ nm) following UV irradiation of jet-cooled 2-bromothiophene at $\lambda =$ (a) 265 nm, (b) 255 nm, and (c) 245 nm. The photolysis laser polarization vector (ϵ) is vertical in the plane of the images as illustrated in panel (a).

This recoil anisotropy matches that of the fast $\text{C}_4\text{H}_3\text{S}^+$ ions. Unlike the latter, however, it cannot be explained simply in terms of axial recoil and the alignment of the transition dipole moment along the breaking C–Br bond, but it does hint that the recoil of both major fragment ions is linked. This suggestion is reinforced by the similar behaviour of the m/z 83 and 39 images upon increasing photon energy. The C_3H_3^+ ion image observed at $\lambda = 255$ nm appears elliptical (Fig. 4(b)) while, by $\lambda = 245$ nm, it is completely isotropic (Fig. 4(c)). Although this behaviour is qualitatively identical to that shown by the $\text{C}_4\text{H}_3\text{S}^+$ ions, we note that the “slow” component is dominant in the C_3H_3^+ images measured at all wavelengths, and that the trend towards slow, isotropic fragments is more abrupt and complete in the case of the C_3H_3^+ fragments. In Section III E we argue that these observations are the result of VUV laser-induced dissociative ionization of the most internally excited (and thus the slowest) $\text{C}_4\text{H}_3\text{S}$ fragments.

Ion images for the minor fragment ion channels labelled in Fig. 3 can also be teased out of the event list recorded by the PImMS2 sensor. Ion images for CS^+ (m/z 44) formed following photolysis at wavelengths of 265, 255, and 245 nm are presented in Figs. 5(a)–5(c). Each CS^+ ion image appears very similar to that recorded for C_3H_3^+ at the same photolysis wavelength, albeit at a significantly lower signal level. As above, these observations would be consistent with dissociative ionization of the $\text{C}_4\text{H}_3\text{S}$ fragments via a (far less competitive) pathway yielding $\text{C}_3\text{H}_3 + \text{CS}^+$ products. This minor channel went unnoticed during the “on-the-fly” observation of live, shot-to-shot data during acquisition but was discovered during analysis—highlighting another strength of event triggered sensors such as PImMS2 where images are recorded for all detectable ions. The images of the HCCS^+ (m/z 57) and H_2CCS^+ (m/z 58) ions are included in Section B of the [supplementary material](#). The HCCS^+ ion images appear generally isotropic although there is some tentative evidence for a weak parallel anisotropy, while the H_2CCS^+ images clearly result from slow-moving species.

Ion images were also recorded for the atomic bromine fragments in their $^2\text{P}_{3/2}$ (Br) and $^2\text{P}_{1/2}$ (Br*) spin-orbit states. These “one-color” experiments employed only the dye laser and the necessary wavelengths for (2 + 1) REMPI detection of Br/Br* also constituted the 2-bromothiophene photolysis wavelength. These images are identical to those reported previously⁴⁵ and are presented in Fig. S4 of Section C in the [supplementary material](#). The momentum distributions extracted from the Br/Br* ion images in Fig. S4 are normalized to their maximum intensities and plotted in Fig. 6 (green and

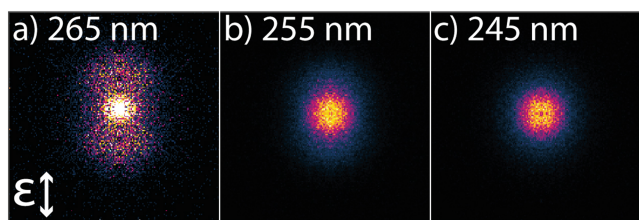


FIG. 5. Velocity-map images of the CS^+ ions detected by VUV ionization ($\lambda = 118$ nm) following UV irradiation of jet-cooled 2-bromothiophene at $\lambda =$ (a) 265 nm, (b) 255 nm and (c) 245 nm. The photolysis laser polarization vector (ϵ) is vertical in the plane of the images and illustrated in panel (a).

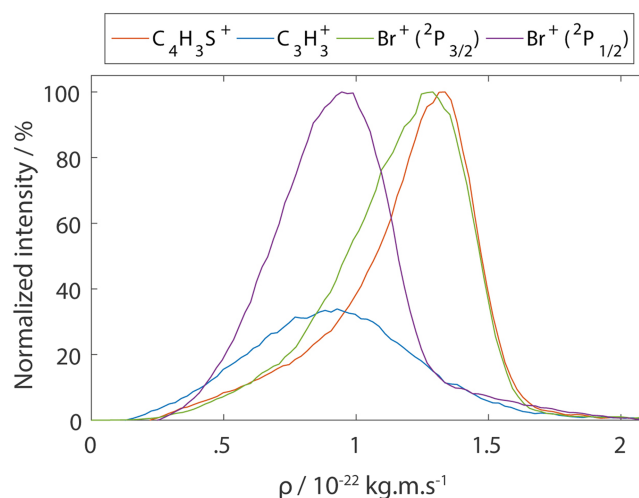


FIG. 6. Momentum distributions derived from ion images for $\text{C}_4\text{H}_3\text{S}^+$ and C_3H_3^+ detected (VUV ionization) simultaneously following UV ($\lambda = 265$ nm) photolysis of jet-cooled 2-bromothiophene compared to those acquired separately for the Br ($^2\text{P}_{3/2}$) and Br ($^2\text{P}_{1/2}$) fragments formed by photolysis at the atomic bromine (2 + 1) REMPI wavelengths of 260.6 and 262.5 nm, respectively.

purple lines, respectively) alongside those extracted from the $\text{C}_4\text{H}_3\text{S}^+$ (orange) and C_3H_3^+ (blue) images (Figs. 3(a) and 4(a)) and normalized (by area) to their branching fractions in Fig. 2. Although these data were acquired at slightly different photolysis wavelengths (260.6 nm (Br), 262.5 nm (Br*), and 265 nm ($\text{C}_4\text{H}_3\text{S}^+$ and C_3H_3^+)), the respective photon energies span a range of just 1.7% that is unlikely to be discernible within the ultimate velocity resolution of the experiment.

Upon examining Fig. 6, the agreement between the high momentum components of the $\text{C}_4\text{H}_3\text{S}$ and Br distributions is immediately clear. Such momentum matching should be expected for two species recoiling from the same prompt photodissociation event, and the observation provides further compelling evidence that these $\text{C}_4\text{H}_3\text{S}$ fragments arise via homolytic C–Br bond cleavage. The Br* fragments are observed at considerably lower momenta, consistent with the additional 0.457 eV of spin-orbit excitation energy.⁶³ The high momentum edge of its distribution overlaps the low momentum tail of the Br and $\text{C}_4\text{H}_3\text{S}$ data, and there is no evidence that the latter contains any substantial contribution from momentum matched Br* + $\text{C}_4\text{H}_3\text{S}$ products. This suggests that the formation of Br* is a minor photodissociation pathway at the UV wavelengths investigated.

One feature of particular note in Fig. 6 is the apparent under-detection of the slower-moving $\text{C}_4\text{H}_3\text{S}$ fragments. If their formation is dominated by C–Br homolysis yielding Br ($^2\text{P}_{3/2}$) co-fragments, the $\text{C}_4\text{H}_3\text{S}$ and Br momentum distributions should match. As discussed in Section III E, this obvious discrepancy can be explained if the most internally excited (and thus translationally slowest) $\text{C}_4\text{H}_3\text{S}$ species undergo dissociative ionization to C_3H_3^+ and CS following irradiation with the $\lambda = 118$ nm probe laser. The blue trace in Fig. 6 shows the momentum distribution of the C_3H_3^+ ion, calculated using the velocity distribution from the image (Fig. 4) and the mass of the thiophenyl radical (83.13 Da), i.e., assuming that the velocities of the C_3H_3^+ ions are largely determined by that of the primary $\text{C}_4\text{H}_3\text{S}$ fragments from which

they derive. Since the $\text{C}_4\text{H}_3\text{S}^+$ and C_3H_3^+ ion images and TOF-MS data were recorded in the same experiment, it is reasonable to scale the area of the normalized radial integration of the C_3H_3^+ image to its branching fraction in Fig. 2. Clearly, the momentum distribution of the C_3H_3^+ ions is likely to be broadened by the dissociative ionization process, but it is reassuring that the centre of this distribution in Fig. 6 appears in the region where slower-moving $\text{C}_4\text{H}_3\text{S}$ fragments are under-detected relative to their momentum-matched Br counterparts.

C. Energetics calculations

It is assumed that the aforementioned dissociative ionization process proceeds by the initial ionization of $\text{C}_4\text{H}_3\text{S}$ followed by the elimination of CS from the cation. The

even-electron loss of CS from $\text{C}_4\text{H}_3\text{S}^+$ can be considered the reverse of an ion-molecule reaction (i.e., $\text{C}_3\text{H}_3^+ + \text{CS} \rightarrow \text{C}_4\text{H}_3\text{S}^+$) and is expected to be barrierless. There are many conceivable pathways by which a terminal R-CS or R-SC group can be formed from ring-opened or intact $\text{C}_4\text{H}_3\text{S}^+$ ions, all largely driven by intramolecular H-atom migration and/or bond rotation. Preliminary calculations suggest that, in the direction of forming a linear propargyl cation (H_2CCCH^+) and CS, these transition states and intermediates will lie at energies considerably below that of the product asymptote. However, similar low energy pathways could not be located for the formation of the more stable cyclopropenyl cation. Therefore, we take the calculated energy threshold for forming C_3H_3^+ ions as the enthalpy of the $\text{C}_4\text{H}_3\text{S} \rightarrow \text{H}_2\text{CCCH}^+ + \text{CS}$ reaction.

Fig. 7 presents the calculated ground-state energies for two dissociative (CS-loss) ionization channels alongside the

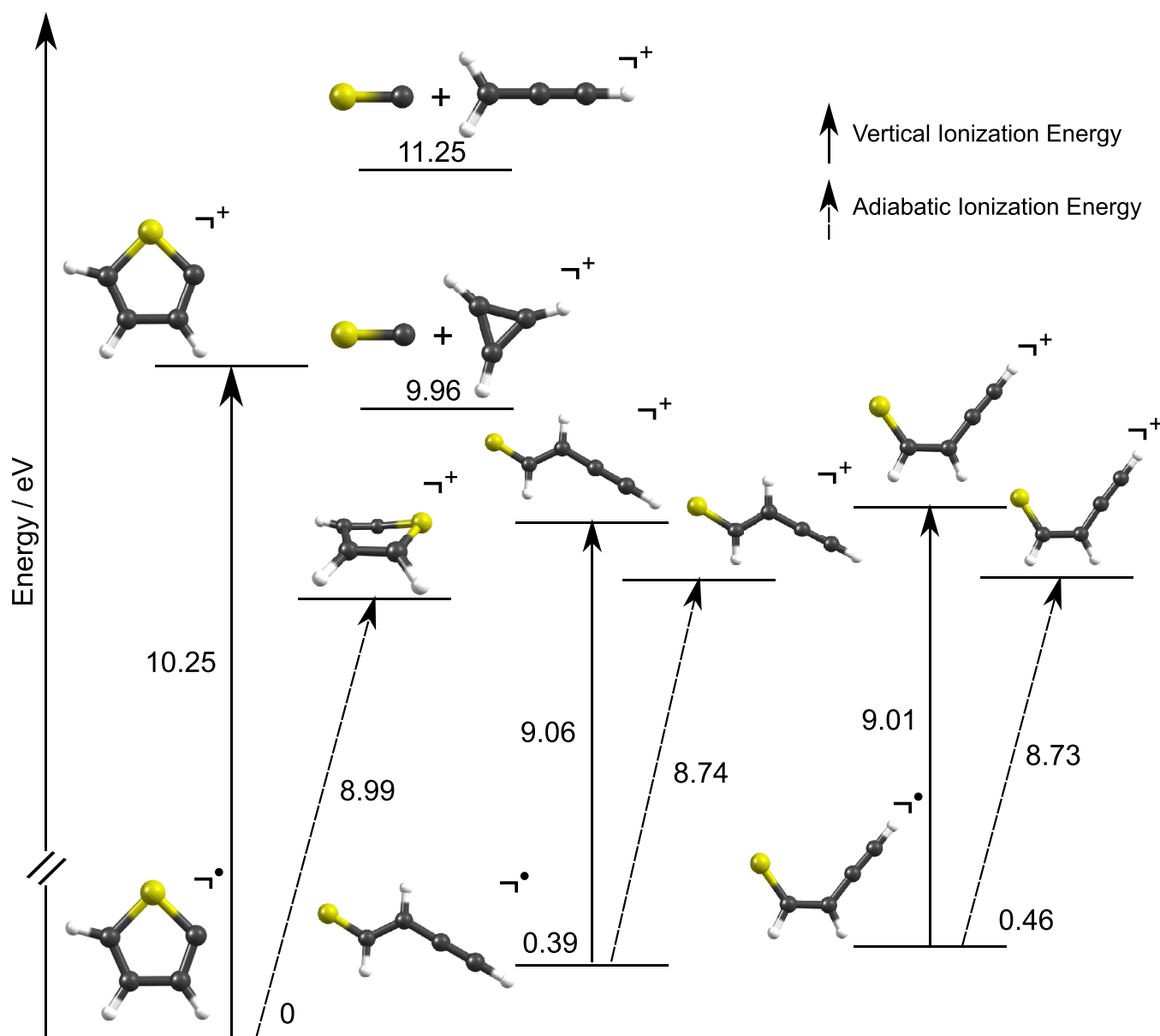


FIG. 7. RI-MP2/def2-TZVP minimum energy geometries and associated CCSD(T)-(F12*)/aug-cc-PVTZ energies for several stable structures on the $\text{C}_4\text{H}_3\text{S}/\text{C}_4\text{H}_3\text{S}^+$ potential energy surface. The energies of these structures are shown (in eV) relative to that of the ground state thiophenyl radical (lower left).

ionization potentials for the intact and two ring-opened isomers of the C_4H_3S radical. The energies of the stationary points are defined relative to that of the thiophenyl radical positioned in the lower left of the figure. Vertical and adiabatic ionization energies are indicated with solid and dashed lines, respectively. First, the vertical IP of the ring-closed thiophenyl radical is predicted to be 10.25 eV and within the energy of a probe laser photon (10.5 eV). The calculated ionization potentials for both the *cis* (9.01 eV) and *trans* (9.06 eV) ring-opened isomers also satisfy this criterion. These ring-opened neutral species are calculated to lie 0.46 and 0.39 eV higher in energy than the global minimum. Dissociative ionization yielding the cyclopropenyl cation within this model has an enthalpy of 9.96 eV, which is close to (but still below that of) the 10.5 eV photon energy. This channel is discounted, however, on the basis that it likely involves significant rearrangement through higher energy barriers and intermediates. The channel yielding $CS + H_2CCCH^+$ is forecast to have an enthalpy of 11.25 eV. This is ~ 0.75 eV greater than the photon energy of the ionization laser—a point to which we return in Section III E.

D. C–Br bond dissociation dynamics

The results of the present study agree well with previous work⁴⁵ and provide much complementary information to support pre-existing models for the near ultraviolet photochemistry of 2-bromothiophene. The velocity-map images measured for the C_4H_3S radical (Fig. 3) and the TKER distributions derived therefrom bear remarkable resemblance to those reported elsewhere from imaging studies of the corresponding Br atom fragment at similar photolysis wavelengths. The trend towards isotropic, slow photoproducts at shorter wavelengths is consistent between the two fragments, which are also momentum matched (Fig. 6). However, this multi-mass study has done more than just highlighting a common origin for the C_4H_3S and Br species. The translational energy information contained in the lighter masses further support conclusions drawn from monitoring the direct C–Br bond fission products. It is noted, both in this study and in others before it,⁴⁵ that the mean TKER of the faster products of primary C–Br bond fission is largely insensitive to increases in photon energy. This is evident in Fig. 3, where the “fast” products are centred at TKER ~ 6000 cm^{-1} at all photolysis wavelengths. This observation, as well as the growth and eventual dominance of a translationally slow channel, leads to the conclusion that an increase in photon energy must lead to a greater partitioning of energy into the internal degrees of freedom of the C_4H_3S product.

This effect manifests itself throughout the experimental data presented here. Most strikingly, it is revealed through the formation of the lighter fragment ions ($C_3H_3^+$ and CS^+) attributable to dissociative ionization of internally excited C_4H_3S fragments which becomes more competitive as the photolysis wavelength is reduced. This is illustrated in Fig. 2. A more subtle clue, discussed further in Sec. III E, lies in the under-detection of slow-moving C_4H_3S fragments as revealed by comparing the momentum distributions shown by the green (Br^+) and orange ($C_4H_3S^+$) traces in Fig. 6.

From the $C_4H_3S^+$ ion images, C–Br bond dissociation energies can also be measured. Consider the relation

$$E_{\text{int}} = h\nu - D_0(C - Br) - \text{TKER}, \quad (1)$$

where E_{int} is the fragment internal energy, $h\nu$ is the photon energy, and $D_0(C-Br)$ is the C–Br bond dissociation energy. The latter can be determined from the TKER distributions in Fig. 3 where prompt, homolytic bond cleavage is dominant and reliable values for TKER_{max} can be estimated, i.e., Figs. 3(a)–3(c). This is because $E_{\text{int}} = 0$ when $\text{TKER} = \text{TKER}_{\text{max}}$ and solving the relationship for $D_0(C-Br)$ becomes trivial. The three $D_0(C-Br)$ values determined in this way all lie within the range $D_0(C-Br) = 28\,640 \pm 320$ cm^{-1} , which we hereby report as the C–Br bond dissociation energy for 2-bromothiophene and is close to the existing literature value of $\sim 29\,000$ cm^{-1} .⁴⁵

Lastly, examining these two momentum distributions alongside that derived from measurements of the Br^* fragment provides some insight into the relative branching into the $C_4H_3S + Br/Br^*$ product channels. As noted above, the high momentum component of the C_4H_3S fragment distribution matches well with that of the Br fragment. The low momentum region is depressed, however, on account of the aforementioned dissociative ionization process. Yet there is no clear evidence that the C_4H_3S momentum distribution might be convolved with contributions from both bromine spin-orbit states. Any significant $C_4H_3S + Br^*$ product yield should be clearly discernible, as the Br^* momentum distribution peaks where that of C_4H_3S is decreasing. Nonetheless, Br^* fragments are detected by 2 + 1 REMPI at the appropriate excitation wavelengths and must be a minor product. This can be rationalised, qualitatively at least, by inspecting previously reported spin-orbit resolved potential energy curves along the C–Br stretch coordinate.⁴⁵ These show that the dissociative, excited electronic states that might channel 2-bromothiophene towards Br^* products intersect the optically “bright” $\pi\pi^*$ states at substantially higher energies than those correlating to Br products.

E. Dissociative ionization of photolysis products

As the photolysis wavelength is reduced, we observe a linear increase in the relative yield of $C_3H_3^+$ ions formed following $\lambda = 118$ nm photoionization of the products of 2-bromothiophene photolysis. This increase comes proportionally at the expense of a signal from the directly ionized C–Br bond homolysis product, $C_4H_3S^+$. This we ascribe to dissociative ionization of the C_4H_3S fragments by the 118 nm probe laser. Comparing the momentum distributions of the $C_4H_3S^+$ and $C_3H_3^+$ ions with that of the ionized ground state Br atoms (all shown in Fig. 6) provides strong support for this interpretation. Being the products of a prompt bond fission, the C_4H_3S and Br momentum distributions should overlap. This is true for the $C_4H_3S^+$ and Br^+ traces (orange and green) at high momenta, where the leading edge of the two distributions matches very well. However, Br^+ is detected across a greater range of momenta, implying under-detection of the slower-moving $C_4H_3S^+$ co-fragments. This can be understood if the most internally activated $C_4H_3S^+$ fragments,

which have the least momentum, are able to access a dissociative ionization channel yielding $\text{C}_3\text{H}_3^+ + \text{CS}$ products. The velocity-map images recorded for C_3H_3^+ (Fig. 4) support this conclusion. These images are similar to those recorded at equivalent wavelengths for the $\text{C}_4\text{H}_3\text{S}^+$ products. They exhibit the same recoil anisotropies, and a greater weighting of intensity towards the lower velocities (i.e., the centre of the image). Assuming that the velocity of this lighter mass fragment is mainly derived from the initial C-Br bond homolysis event, with some (smaller) statistical contribution from the dissociative ionization step, allows its momentum distribution to be estimated by treating it as if it had the mass of its $\text{C}_4\text{H}_3\text{S}$ progenitor. The resulting C_3H_3^+ momentum distribution, given by the blue trace in Fig. 6, is centred within the region where the Br and $\text{C}_4\text{H}_3\text{S}$ momentum distributions disagree.

Isomerization on the cation potential energy surface towards a ring-opened species with a terminal CS group followed by elimination of CS to form a propargyl cation is a probable pathway for the dissociative ionization. The calculated energetics predict this channel to have an overall enthalpy of 11.25 eV (Fig. 7). If the energies of the intermediates and transition states all lie below that of the asymptotic products, this would mean that the dissociative ionization of $\text{C}_4\text{H}_3\text{S}$ radicals to $\text{C}_3\text{H}_3^+ + \text{CS}$ products requires that the radicals have an internal energy $E_{\text{int}} \geq 0.75$ eV prior to excitation by the probe laser (10.5 eV). According to Equation (1), at $\lambda = 265$ nm, for example, $\text{C}_4\text{H}_3\text{S}$ fragments with a corresponding TKER $< \sim 3000 \text{ cm}^{-1}$ will have $E_{\text{int}} > 0.75$ eV. This constitutes $\sim 24\%$ of the TKER distribution determined from the Br ion image recorded with a photolysis wavelength near 265 nm (Fig. S4 of the [supplementary material](#)). Note that the fraction of the TKER distribution with the requisite internal energy for dissociative ionization (24%) is similar to the branching fraction for the C_3H_3^+ channel reported in Fig. 2 ($\sim 25\%$ – 33%). This TKER boundary for dissociative ionization rises as the photon energy is increased. At $\lambda = 255$ nm, $\text{C}_4\text{H}_3\text{S}$ fragments with a corresponding TKER $< 4500 \text{ cm}^{-1}$ will have $E_{\text{int}} > 0.75$ eV, while by $\lambda = 245$ nm the threshold has increased to TKER $< 6100 \text{ cm}^{-1}$. The likelihood of dissociative ionization at the shorter photolysis wavelengths is enhanced not just by the increased photon energy but also by the increased probability of parent fragmentation into a translationally slow product channel. The minor CS^+ ion channel exhibits similar behaviour, leading to similar ion images (Fig. 5) and a tentative trend that increases with photon energy shown as the green data points in Fig. 2. However, this remains a minority pathway, detected at low signal levels, at all photolysis wavelengths investigated.

IV. CONCLUSION

Multi-mass velocity-map imaging, coupled with VUV universal ionization, has been used to study the near ultraviolet photochemistry of 2-bromothiophene in the wavelength range 265–245 nm. Ion images have been analyzed for the molecular $\text{C}_4\text{H}_3\text{S}$ fragment resulting from prompt C–Br bond homolysis. These reveal a fast, anisotropic bond fission process at the lower photon energies within this range, which is superseded

by a process yielding an isotropic distribution of translationally slow $\text{C}_4\text{H}_3\text{S}$ fragments at higher photon energies. These findings are in agreement with the findings of a previous study that imaged the atomic Br fragments and, additionally, identify that most of these atoms are formed in their ground ($^2\text{P}_{3/2}$) spin-orbit state. However, the present study also detected a number of lighter product ions, including a dominant C_3H_3^+ ion that was particularly prevalent at short photolysis wavelengths. Drawing from the ion images acquired simultaneously for multiple channels, and from *ab initio* calculations, this fragment ion has been attributed to dissociative ionization (by the VUV probe laser) of the most internally excited $\text{C}_4\text{H}_3\text{S}$ photofragments. Photoionization using 118 nm photons would often be viewed as a “soft” ionization method, yet in the present experiments it is often responsible for the majority of the total fragment ion current. Nonetheless, since the photon energies are well defined, it is possible to unravel such processes and to gain new insights into the energetics of the neutral and/or ion fragmentation processes. The present study provides an excellent demonstration of the development and use of event-triggered, high frame rate sensors for VMI. We end by reiterating the point that, though good scientific practice demands repeats of any given experiment, all of the universal ionization data used to prepare this paper derive from just one experiment at each photolysis wavelength, i.e., a total of five experimental acquisitions.

SUPPLEMENTARY MATERIAL

See [supplementary material](#) for an overview of the preliminary VMI data acquired prior to commencing this universal ionization multi-mass study, the ion images detected for HCCS^+ and H_2CCS^+ at $\lambda = 265$ nm, 255 nm, and 245 nm and for the atomic bromine ion images recorded using (2 + 1) REMPI following 260.6/262.5 nm photolysis.

ACKNOWLEDGMENTS

The authors are grateful to Dr. B. Marchetti and Dr. T. N. V. Karsili for their contributions during the early stages of this work. The authors also enjoy a productive collaboration with Photek Limited that delivers customized detector solutions. This project is funded by EPSRC Programme Grant No. EP/L005913. The raw ion events data and calculation log files can be retrieved from the University of Bristol’s research data repository and can be accessed using the following DOI: [10.5523/bris.k35bi3pqsdh2b5moo2e3puxf](https://doi.org/10.5523/bris.k35bi3pqsdh2b5moo2e3puxf).

- ¹A. T. J. B. Eppink and D. H. Parker, *Rev. Sci. Instrum.* **68**, 3477–3484 (1997).
- ²M. N. R. Ashfold, N. H. Nahler, A. J. Orr-Ewing, O. P. J. Vieuxmaire, R. L. Toomes, T. N. Kitsopoulos, I. A. Garcia, D. A. Chestakov, S.-M. Wu, and D. H. Parker, *Phys. Chem. Chem. Phys.* **8**, 26–53 (2006).
- ³A. I. Chichinin, K.-H. Gericke, S. Kauczok, and C. Maul, *Int. Rev. Phys. Chem.* **28**, 607–680 (2009).
- ⁴M. N. R. Ashfold, G. A. King, D. Murdock, M. G. D. Nix, T. A. A. Oliver, and A. G. Sage, *Phys. Chem. Chem. Phys.* **12**, 1218–1238 (2010).
- ⁵A. G. Sage, T. A. A. Oliver, D. Murdock, M. B. Crow, G. A. D. Ritchie, J. N. Harvey, and M. N. R. Ashfold, *Phys. Chem. Chem. Phys.* **13**, 8075–8093 (2011).
- ⁶K. L. K. Lee, K. Nauta, and S. H. Kable, *J. Chem. Phys.* **146**, 044304 (2017).

- ⁷S. M. Poullain, D. V. Chicharro, A. Zanchet, M. G. Gonzalez, L. Rubio-Lago, M. L. Senent, A. Garcia-Vela, and L. Banares, *Phys. Chem. Chem. Phys.* **18**, 17054–17061 (2016).
- ⁸S. J. Greaves, R. A. Rose, and A. J. Orr-Ewing, *Phys. Chem. Chem. Phys.* **12**, 9129–9143 (2010).
- ⁹K. Honma and D. Hirata, *J. Chem. Phys.* **147**, 013903 (2017).
- ¹⁰S. Pandit, B. Hornung, G. T. Dunning, T. J. Preston, K. Brazener, and A. J. Orr-Ewing, *Phys. Chem. Chem. Phys.* **19**, 1614–1626 (2017).
- ¹¹T. J. Preston, G. T. Dunning, A. J. Orr-Ewing, and S. A. Vázquez, *J. Phys. Chem. A* **118**, 5595–5607 (2014).
- ¹²B. Joalland, Y. Shi, A. Kamasah, A. G. Suits, and A. M. Mebel, *Nat. Commun.* **5**, 1–6 (2014).
- ¹³V. Dribinski, A. Ossaditchi, V. A. Mandelshtam, and H. Reisler, *Rev. Sci. Instrum.* **73**, 2634–2642 (2002).
- ¹⁴A. J. R. Heck and D. W. Chandler, *Annu. Rev. Phys. Chem.* **46**, 335–372 (1995).
- ¹⁵S. Manzhos and H.-P. Looock, *Comput. Phys. Commun.* **154**, 76–87 (2003).
- ¹⁶G. M. Roberts, J. L. Nixon, J. Lecointre, E. Wrede, and J. R. R. Verlet, *Rev. Sci. Instrum.* **80**, 053104 (2009).
- ¹⁷D. A. Chestakov, S.-M. Wu, G. Wu, D. H. Parker, A. T. J. B. Eppink, and T. N. Kitsopoulos, *J. Phys. Chem. A* **108**, 8100–8105 (2004).
- ¹⁸D. Townsend, M. P. Minitti, and A. G. Suits, *Rev. Sci. Instrum.* **74**, 2530–2539 (2003).
- ¹⁹T. Kinugawa and T. Arikawa, *J. Chem. Phys.* **96**, 4801–4804 (1992).
- ²⁰K. Lorenz, D. Chandler, J. Barr, W. Chen, G. Barnes, and J. Cline, *Science* **293**, 2063–2066 (2001).
- ²¹M. A. Young, *J. Chem. Phys.* **102**, 7925–7936 (1995).
- ²²J. J. Lin, J. Zhou, W. Shiu, and K. Liu, *Rev. Sci. Instrum.* **74**, 2495–2500 (2003).
- ²³R. L. Toomes, P. C. Samartzis, T. P. Rakitzis, and T. N. Kitsopoulos, *Chem. Phys.* **301**, 209–212 (2004).
- ²⁴M. L. Lipciuc and M. H. M. Janssen, *Phys. Chem. Chem. Phys.* **8**, 3007–3016 (2006).
- ²⁵A. G. Suits and O. S. Vasyutinskii, *Chem. Rev.* **108**, 3706–3746 (2008).
- ²⁶C. Martin, P. Jelinsky, M. Lampton, R. F. Malina, and H. O. Anger, *Rev. Sci. Instrum.* **52**, 1067–1074 (1981).
- ²⁷J. H. D. Eland and A. H. Pearson, *Meas. Sci. Technol.* **1**, 36 (1990).
- ²⁸O. Jagutzki, V. Mergel, K. Ullmann-Pfleger, L. Spielberger, U. Spillmann, R. Dörner, and H. Schmidt-Böcking, *Nucl. Instrum. Methods Phys. Res., Sect. A* **477**, 244–249 (2002).
- ²⁹K. Motomura, L. Foucar, A. Czasch, N. Saito, O. Jagutzki, H. Schmidt-Böcking, R. Dörner, X.-J. Liu, H. Fukuzawa, G. Prümper, K. Ueda, M. Okunishi, K. Shimada, T. Harada, M. Toyoda, M. Yanagihara, M. Yamamoto, H. Iwayama, K. Nagaya, M. Yao, A. Rudenko, J. Ullrich, M. Nagasono, A. Higashiya, M. Yabashi, T. Ishikawa, H. Ohashi, and H. Kimura, *Nucl. Instrum. Methods Phys. Res., Sect. A* **606**, 770–773 (2009).
- ³⁰W. F. Kosonocky, G. Yang, R. K. Kabra, C. Ye, Z. Pektas, J. L. Lowrance, V. J. Mastrocola, F. V. Shallcross, and V. Patel, *IEEE Trans. Electron Devices* **44**, 1617–1624 (1997).
- ³¹T. G. Etoh, D. Poggemann, G. Kreider, H. Mutoh, A. J. P. Theuwissen, A. Ruckelshausen, Y. Kondo, H. Maruno, K. Takubo, H. Soya, K. Takehara, T. Okinaka, and Y. Takano, *IEEE Trans. Electron Devices* **50**, 144–151 (2003).
- ³²Z. Amitay and D. Zajfman, *Rev. Sci. Instrum.* **68**, 1387–1392 (1997).
- ³³S. K. Lee, F. Cudry, Y. F. Lin, S. Lingenfelter, A. H. Winney, L. Fan, and W. Li, *Rev. Sci. Instrum.* **85**, 123303 (2014).
- ³⁴J. J. John, M. Brouard, A. Clark, J. Crooks, E. Halford, L. Hill, J. W. L. Lee, A. Nomerotski, R. Pisarczyk, I. Sedgwick, C. S. Slater, R. Turchetta, C. Vallance, E. Wilman, B. Winter, and W. H. Yuen, *J. Instrum.* **7**, C08001 (2012).
- ³⁵X. Llopert, R. Ballabriga, M. Campbell, L. Tlustos, and W. Wong, *Nucl. Instrum. Methods Phys. Res., Sect. A* **581**, 485–494 (2007).
- ³⁶M. Brouard, E. K. Campbell, A. J. Johnsen, C. Vallance, W. H. Yuen, and A. Nomerotski, *Rev. Sci. Instrum.* **79**, 123115 (2008).
- ³⁷K. Amini, S. Blake, M. Brouard, M. B. Burt, E. Halford, A. Lauer, C. S. Slater, J. W. L. Lee, and C. Vallance, *Rev. Sci. Instrum.* **86**, 103113 (2015).
- ³⁸S. H. Gardiner, M. L. Lipciuc, T. N. V. Karsili, M. N. R. Ashfold, and C. Vallance, *Phys. Chem. Chem. Phys.* **17**, 4096–4106 (2015).
- ³⁹A. T. Clark, J. P. Crooks, I. Sedgwick, R. Turchetta, J. W. L. Lee, J. J. John, E. S. Wilman, L. Hill, E. Halford, C. S. Slater, B. Winter, W. H. Yuen, S. H. Gardiner, M. L. Lipciuc, M. Brouard, A. Nomerotski, and C. Vallance, *J. Phys. Chem.* **116**, 10897–10903 (2012).
- ⁴⁰M. N. R. Ashfold and J. D. Howe, *Annu. Rev. Phys. Chem.* **45**, 57–82 (1994).
- ⁴¹R. L. Gross, X. Liu, and A. G. Suits, *Chem. Phys. Lett.* **362**, 229–234 (2002).
- ⁴²D. Townsend, W. Li, S. K. Lee, R. L. Gross, and A. G. Suits, *J. Phys. Chem. A* **109**, 8661–8674 (2005).
- ⁴³S.-T. Tsai, C.-K. Lin, Y. T. Lee, and C.-K. Ni, *Rev. Sci. Instrum.* **72**, 1963–1969 (2001).
- ⁴⁴H. Fan and S. T. Pratt, *J. Chem. Phys.* **123**, 204301 (2005).
- ⁴⁵B. Marchetti, T. N. V. Karsili, O. Kelly, P. Kapetanopoulos, and M. N. R. Ashfold, *J. Chem. Phys.* **142**, 224303 (2015).
- ⁴⁶N. Gavrilov, S. Salzmann, and C. M. Marian, *Chem. Phys.* **349**, 269–277 (2008).
- ⁴⁷S. Salzmann, M. Kleinschmidt, J. Tatchen, R. Weinkauff, and C. M. Marian, *Phys. Chem. Chem. Phys.* **10**, 380–392 (2008).
- ⁴⁸M. Stenrup, *Chem. Phys.* **397**, 18–25 (2012).
- ⁴⁹R. A. Ingle, T. N. V. Karsili, G. J. Dennis, M. Staniforth, V. G. Stavros, and M. N. R. Ashfold, *Phys. Chem. Chem. Phys.* **18**, 11401–11410 (2016).
- ⁵⁰D. Murdock, S. J. Harris, J. Luke, M. P. Grubb, A. J. Orr-Ewing, and M. N. R. Ashfold, *Phys. Chem. Chem. Phys.* **16**, 21271–21279 (2014).
- ⁵¹D. Murdock, R. A. Ingle, I. V. Sazanovich, I. P. Clark, Y. Harabuchi, T. Taketsugu, S. Maeda, A. Orr-Ewing, and M. N. R. Ashfold, *Phys. Chem. Chem. Phys.* **18**, 2629–2638 (2016).
- ⁵²F. Zhang, Z. Cao, X. Qin, Y. Liu, Y. Wang, and B. Zhang, *Acta Phys.-Chim. Sin.* **24**, 1335–1341 (2008).
- ⁵³E. Wrede, S. Laubach, S. Schulenburg, A. Brown, E. R. Wouters, A. J. Orr-Ewing, and M. N. R. Ashfold, *J. Chem. Phys.* **114**, 2629–2646 (2001).
- ⁵⁴W. S. Hopkins, M. L. Lipciuc, S. H. Gardiner, and C. Vallance, *J. Chem. Phys.* **135**, 034308 (2011).
- ⁵⁵Slimer, <http://www.bristoldynamics.com/resources/>.
- ⁵⁶C. Hättig, A. Hellweg, and A. Köhn, *Phys. Chem. Chem. Phys.* **8**, 1159–1169 (2006).
- ⁵⁷F. Weigend and M. Häser, *Theor. Chem. Acc.* **97**, 331–340 (1997).
- ⁵⁸A. Schäfer, C. Huber, and R. Ahlrichs, *J. Chem. Phys.* **100**, 5829 (1994).
- ⁵⁹TURBOMOLE V6.2 2010, A development of University of Karlsruhe and Forschungszentrum Karlsruhe GmbH, 1989–2007, TURBOMOLE GmbH, since 2007, available from <http://www.turbomole.com>.
- ⁶⁰H.-J. Werner, P. J. Knowles, G. Knizia, F. R. Manby, M. Schütz, P. Celani, W. Györfy, D. Kats, T. Korona, R. Lindh, A. Mitrushenkov, G. Rauhut, K. R. Shamasundar, T. B. Adler, R. D. Amos, A. Bernhardsson, A. Berning, D. L. Cooper, M. J. O. Deegan, A. J. Dobbyn, F. Eckert, E. Goll, C. Hampel, A. Hesselmann, G. Hetzer, T. Hrenar, G. Jansen, C. Köppl, Y. Liu, A. W. Lloyd, R. A. Mata, A. J. May, S. J. McNicholas, W. Meyer, M. E. Mura, A. Nicklass, D. P. O’Neill, P. Palmieri, D. Peng, K. Pflüger, R. Pitzer, M. Reiher, T. Shiozaki, H. Stoll, A. J. Stone, R. Tarroni, T. Thorsteinsson, and M. Wang, MOLPRO, version 2015.1, a package of *ab initio* programs, 2015, see <http://www.molpro.net>.
- ⁶¹T. B. Adler, G. Knizia, and H.-J. Werner, *J. Chem. Phys.* **127**, 221106 (2007).
- ⁶²G. Knizia, T. B. Adler, and H. J. Werner, *J. Chem. Phys.* **130**, 054104 (2009).
- ⁶³A. Kramida, Yu. Ralchenko, J. Reader, and NIST ASD Team, *NIST Atomic Spectra Database*, version 5.4 (National Institute of Standards and Technology, Gaithersburg, MD, 2016), available, online, <http://physics.nist.gov/asd>, Tue Feb 22 2017.